Design and Optimization of an Improved T-shape Linear Permanent Magnet Machines

Rong Guo* and Wei He

School of Electrical and Information Engineering, Beijing University of Civil Engineering and Architecture, Beijing 100044, China

This paper presents an improved T-shape linear permanent magnet machine (T-LPMM) based on a traditional surface-mounted linear permanent magnet machine (SM-LPMM). The proposed topological structure aims to protect the surface of the permanent magnet from corrosion and enhance the rigidity against make high-frequency vibration. Firstly, the slotless magnetic field is predicted using finite-element method (FEM) with automatic scripting in MATLAB to consider the inset T-shape structure of PM. Then, the Schwarz-Christoffel (SC) mapping is adopted to calculate the slot effect. Afterward, a subdomain (SD) model is established to analyze the armature reaction, and Taguchi method is employed for optimization purposes. The optimized result is verified by FEM, and a comparison experiment is conducted between T-LPMM and SM-LPMM. The experimental demonstrate superior electromagnetic output performance of the proposed T-LPMM.

Keywords : T-shape PM, linear permanent magnet machine, analysis method, magnetic field

1. Introduction

Linear permanent magnet machines (LPMMs) have been widely application in industry such as wave power generation, aerospace etc. [1-3]. Generally, according to the position of permanent magnets, the linear machine can be classified into two categories: surface-mounted and embedded-mounted [4, 5]. Radial and Halbach magnetization are mainly used for surface-mounted permanent magnet linear machine [6-9]. In [7], a novel linear generator topology is proposed with no magnetic attraction force between stator and PM mover. The proposed linear generator can reduce mass and simplifies assembly. The GA optimization method is used to find the most cost-effective design. The experiment result show that the optimized linear machine has an 87.5% average efficiency which is better than conventional iron-core PM linear machine. In [8], a field-modulated tubular linear permanent magnet generator with quasi-Halbach structure is proposed for ocean wave energy conversion. The design is optimized using an analytical method to reduce computation time. The results are verified by FEM

and experiments which show that the output voltage is 43% higher than traditional Halbach linear machine. Embedded permanent magnet linear machines often utilize axially magnetized magnets [10-12]. In [10], axially magnetized permanent magnets are used in tubular linear synchronous machines (TLSMs), aiming to minimize the mass of the iron pole through an optimum magnetic circuit design method that consider leakage flux. The total flux improved by 39.31% compared to conventional machines by selecting an appropriate thickness ratio for the iron poles.

To design and analyze the aforementioned linear machine topologies, various methods are commonly used, including finite element method (FEM), magnetic equivalent circuit method (MEC), and analysis method (AM) [13-16]. FEM provides high accuracy but is time-consuming, while, MEC method offers lower computational costs, although node selection lacks a standardized approach. AMs such as conformal transformation (CT) and subdomain (SD) methods are effective during the initial design step. In [15], a magnetic field reconstruction method for analyzing linear permanent magnet oscillators, considering auxiliary-teeth and slot effects through a two-step Schwarz-Christoffel (SC) conformal transformation method. The analysis results are validated through FEM and experiment data, holding good agreement. In [16], a novel flux-

*Corresponding author: Tel: +86-18813189123
Fax: +86-01061209193, e-mail: guorong@bucea.edu.cn

modulated PM linear machine with a sandwich armature for free-piston energy converter system is presented. An accurate SD model is used to calculate the magnetic field with determination the best pole/slot combination. A prototype with optimized structural parameters is manufactured and tested.

Taking advantages of magnetization and calculation methods, this paper proposed an improved T-shape linear permanent magnet machine (T-LPMM) based on a conventional SM-LPMM, which offers benefits such as high thrust force, low magnetic flux leakage, and ease of maintenance. The paper is organized as follows: In Section 2, the structure and operation principle are described. The magnetic field analysis model which considered slot effect and armature reaction are presented in Section 3. Afterward, in Section 4, the Taguchi method based on analysis model are used to optimize the T-LPMM. The FEM and experiment are conducted to verified the analysis results in Section 5, and conclusions are drawn at the end of the paper.

2. Structure and Principle of T-LPMM

The structure of the proposed T-LPMM is shown in Fig. 1. To reduce the detent force, auxiliary teeth are incorporated at end of the stator iron, additionally, concentrated winding is employed to improve utilization. On the mover side, PMs are magnetized axially and radially, providing advantages such as concentrated magnetic flux, reduced flux leakage, and improved thrust force.
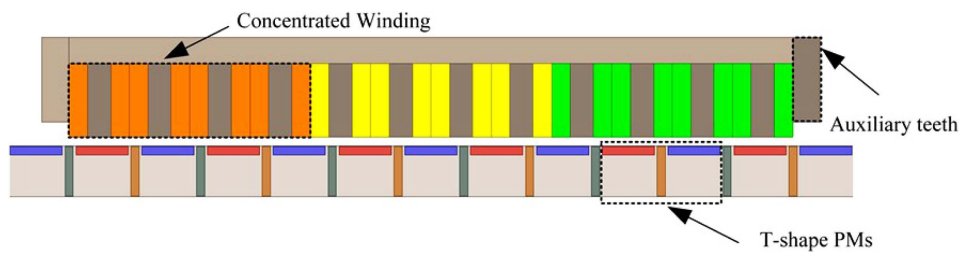
The operation principle of T-LPMM is depicted in Fig. 2. The three-phase armature winding and PMs are the main magnetic circuit. When the mover is positioned at the center of T-LPMM, the total magnetic flux is zero. As the mover moves, the magnetic flux changes, inducing an electromotive force (EMF) and generating the resulting force.

3. Magnetic Field Prediction

3.1. Slotless analysis model
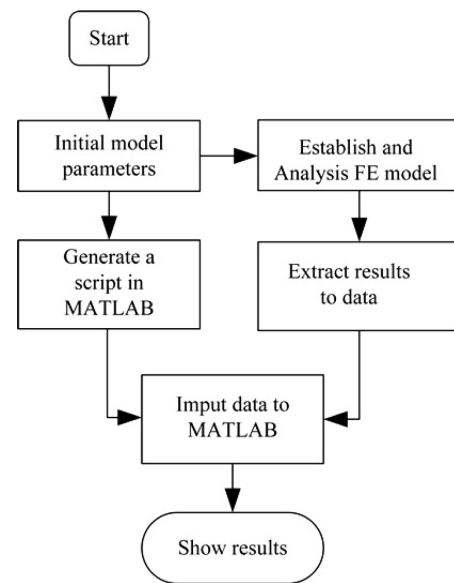
Analyzing the structure of PM in the mover using an

Fig. 3. Calculation process of slotless magnetic field.

Fig. 1. (Color online) Proposed structure of T-LPMM.
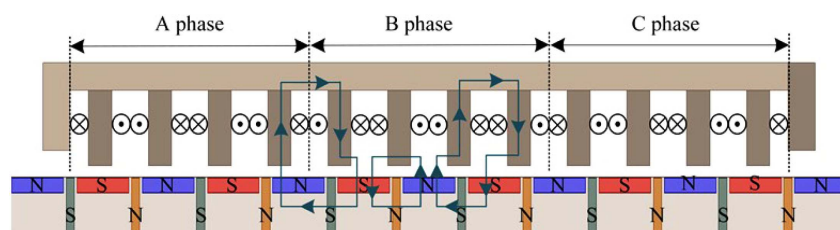
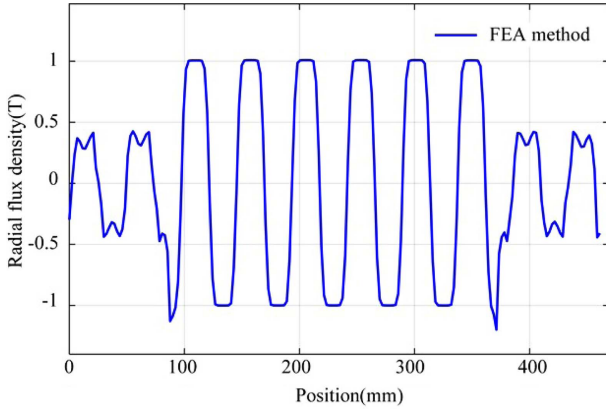**Fig. 2.** (Color online) Operation principle of T-LPMM.

Fig. 4. (Color online) Air-gap flux density distribution under no-load condition.

analytical method involves numerous boundary conditions and solving equations, leading to complexity in calculation. To address this, a slotless model is developed as an intermediary between FEM model and MATLAB. The process of the slotless model is illustrated in Fig. 3. Firstly, scripts are generated in MATLAB based on the parameters of FEM model. Subsequently, a static analysis is performed in FEM model, considering factors such as end and the auxiliary teeth effects. The resulting flux density is then extracted from FEM model into MATLAB using a test file. The distribution of the no-load air-gap flux density is presented in Fig. 4.

3.2. Slot-effect analysis model

Several approaches can be used to consider the slotting effect such as lateral force (LF), subdomain method (SD) and complex permeance (CP) etc. [17-19]. Each method possesses its own advantages and limitations. LF can yield quick results, but neglects the tangential component. SD method can accurately predict the slot effect, but additional boundary conditions are required, which adds computational burden. Complex permeance (CP) method mainly includes traditional conformal mapping (CM) and

SC mapping. CM method offers acceptable accuracy, but limited by geometric structures. Thanks to the SC mapping technique integrated into MATLAB toolbox, the complex structure can be accurately represented. Hence, in this paper, the SC mapping method is carried out to consider the slotting effect as shown in Fig. 5. From Fig. 5, it can be found that a slotted air gap plane can be transformed into a slotless air gap plane via two-step transformation process.

where A and C represent the complex integration coefficient, respectively, q represents the number of polygon vertices in -plane, w is the number of points in the canonical domains, and a_k represents the interior angles. All these parameters can be obtained from SC Toolbox.

To mapping ζ-plane onto a rectangular domain in w-plane, the calculation is expressed as follows:

$$w = g(\zeta) = j(\log(\zeta)\frac{\Delta x}{2\pi} + \frac{\Delta y}{2} - j\frac{\Delta x}{2}) \qquad (1)$$

where,

$$\Delta x = Real\big[w(1)\big] - Real\big[w(4)\big] \quad \Delta y = Imag\big[w(2)\big] - Imag\big[w(1)\big]$$

Finally, the flux density in slot region can be derived using following equations:

$$B_s = B_g \cdot \lambda = \big(B_r + j \cdot B_t\big) \cdot \big(\lambda_r + j\lambda_t\big) \qquad (2)$$

where B_g is the slotless air-gap flux density in SD model, B_r and B_t are the radial and tangential, respectively, under open circuit conditions.

3.3. Armature Reaction Magnetic field

In order to account for the armature reaction in T-LPMM, SD method is used due to its capability of accurate analysis. To simply the calculations, several assumptions are made: 1) The iron permeability of both the stator and mover is assumed to be infinite, neglecting the saturation effect; 2) The magnetic permeability in the magnets is considered constant and denoted as u_r.
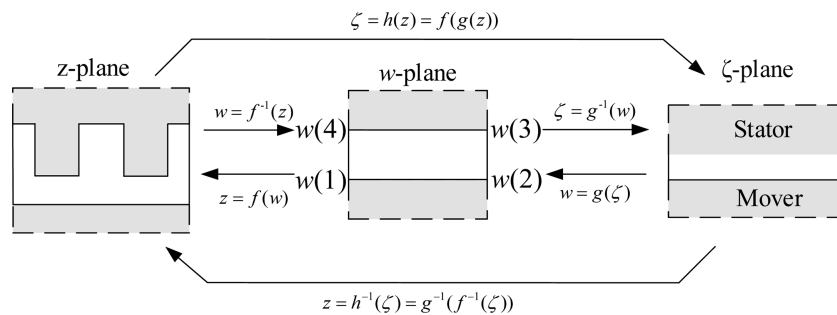

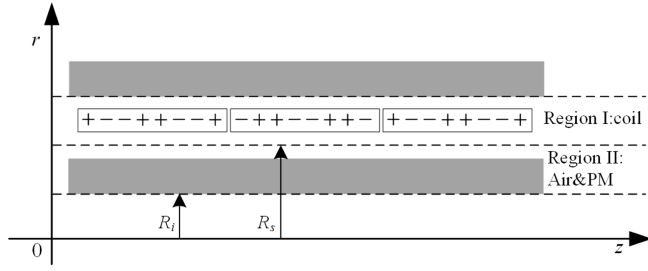**Fig. 5.** Transformation process of SC mapping method.

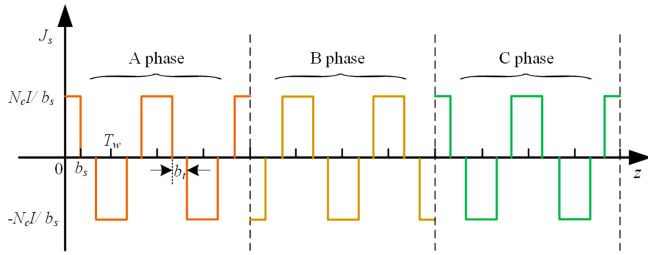**Fig. 6.** Subdomain model of armature reaction.

Fig. 7. (Color online) Equivalent current sheet model of T-LPMM.

The armature reaction field model is depicted in Fig. 6.

The armature reaction magnetic field is primarily generated by the coils. The current distribution in the fractional slot concentrated winding can be predicted using a current sheet model. According to Ampere's law, the ampere-turn current in a slot can be equivalently represented as a current sheet $N_c I/b_s$ distributed over the width of the slot opening b_s at the armature radius R_s. The distribution of the equivalent current sheet is shown in Fig. 7.

From Fig. 6, the current distribution can be expanded into a Fourier series with the following form

$$J_s(z) = \sum_{n=1}^{\infty} J_n \sin m_{an} z \tag{3}$$

where, $m_{an}=n\pi/\tau_{mp}$, τ_{mp} represents the length of stator, and the J_n can be calculated as follows:

$$J_n = \frac{1}{\tau_{mp}} \int_{-\tau_{mp}}^{\tau_{mp}} J_{s(z)} \sin m_{an} z dz \tag{4}$$

For each region, the governing equation for armature reaction field is expressed as follows:

$$\frac{\partial}{\partial z}\left(\frac{1}{r}\frac{\partial}{\partial z}(rA_{\theta 1})\right) + \frac{\partial}{\partial r}\left(\frac{1}{r}\frac{\partial}{\partial r}(rA_{\theta 1})\right) = -u_0 \overrightarrow{J_s} \tag{5}$$

$$\frac{\partial}{\partial z}\left(\frac{1}{r}\frac{\partial}{\partial z}(rA_{\theta 1})\right) + \frac{\partial}{\partial r}\left(\frac{1}{r}\frac{\partial}{\partial r}(rA_{\theta 1})\right) = 0 \tag{6}$$

The corresponding generation solution is obtained as:

$$B_r(r,z) = -\sum_{n=1}^{\infty} [a_{na}BI_1(m_{an}r)\cos(m_{an}z)] \tag{7}$$

$$B_z(r,z) = \sum_{n=1}^{\infty} [a_{na}BI_0(m_{an}r)\sin(m_{an}z)] \tag{8}$$

Where $a_{na} = u_0 J_n \big/ BI_0(m_{an}R_s)$

According to the given boundary conditions, the solution for the flux density in the armature reaction field can be derived as follows:

$$B_z\big|_{r=R_s} = u_0 J_s(z) \tag{9}$$

$$B_r\big|_{r=R_i} = 0 \tag{10}$$

For predict EMF of T-LPMM, the coil flux linkage needs to be calculated the integration formula is given by:

$$\psi_w = \frac{N_c}{2b_s(R_b - R_s)} \int_{z-b_s}^{z-b_s} \int_{R_s}^{R_b} 2\pi r A_{r3}(r,z)drdz \tag{11}$$

Based on the flux linkage, the EMF can be calculated using (30)

$$E_a = -\frac{\partial \psi_w}{\partial t} = -\frac{\partial \psi_w}{\partial \Delta_z}\frac{\partial \Delta_z}{\partial t} = -v_m \frac{\partial \psi_w}{\partial \Delta_z} \tag{12}$$

where, v_m represents the mover speed of T-TPMLM

The analysis of the thrust force for one coil can is based on the derived air-gap flux density, which is given as follows:

$$F_t = \int_{z-b_s}^{z+b_s} \int_{R_s}^{R_b} 2\pi r J B_{r3}(r,z)drdz \tag{13}$$

The thrust force of the entire linear machine can be determined by summing up the forces generated by each individual coil.

4. Optimal design of the T-LPMM

Optimization design is a complicated process, the rationality of parameters directly affects the output performance. Selecting an appropriate optimization method is crucial to save time and improve efficiency. In this paper, based on the analytical model developed earlier, Taguchi optimization method is applied to obtain the optimal parameters for T-LPMM. The following parameters

Table 1. Optimize variables and level factors of T-LPMM.

Variables	Level 1	Level 2	Level 3
L_{pm_1}	15	16	17
w_{pm_k}	2	2.5	3
dy	0	1	2
w_{fx}	28	29	30
h_{fz}	9	10	11

Table 2. Orthogonal experiment matrix of T-LPMM.

No.	Orthogonal arrays					Output Performance	
	L_{pm_1}/mm	w_{pm_k}/mm	dy/mm	w_{fx}/mm	h_{fz}/mm	F_d/N	F_t/N
1	15	2	0	28	10	23.93	91.71
2	15	2.5	1	29	9	25.62	99.00
3	15	3	2	30	11	48.99	220.11
4	16	2	1	30	9	28.68	70.34
5	16	2..5	2	28	10	39.18	158.21
6	16	3	0	29	11	32.75	129.26
7	17	2	2	29	11	29.72	115.87
8	17	2.5	0	30	10	41.44	166.02
9	17	3	1	28	9	33.48	231.62

are identified as the optimized parameters: PM length (L_{pm_1}), PM width (w_{pm_k}), distance between permanent magnets (dy), auxiliary teeth width (w_{Tf}), and auxiliary teeth height (h_{fz}). The optimization objectives are set as minimizing the detent force and maximizing the thrust force. To facilitate the optimization process, a level table for T-LPMM is constructed, as shown in Table 1.

Using traditional methods (e.g., FEM), calculating the design parameters would require 3^5=243 evaluations. However, by employing Taguchi method, only 9 evaluations are required, significantly reducing computational costs. The orthogonal experimental arrays (L_9) are presented

Table 3. Average of T-LPMM.

Parameters	F_d/N	F_t/N
Average values	33.76	142.46

Table 4. Average performance of T-LPMM at different levels.

Parameters	level	F_d/N	F_t/N
L_{pm_1}/mm	1	32.75	136.94
	2	33.54	119.27
	3	34.88	171.17
w_{pm_k}/mm	1	27.44	92.64
	2	35.41	193.66
	3	38.71	141.08
dy/mm	1	32.71	128.99
	2	29.26	133.65
	3	39.29	164.73
w_{fx}/mm	1	32.20	160.51
	2	29.37	114.71
h_{fz}/mm	3	39.70	152.16
	1	34.85	138.65
	2	29.26	133.65
	3	37.16	155.08

in Table 2.

To analyze the influence of the aforementioned factors on the output performance of T-LPMM at different levels, mean value analysis is carried out. The performance for each factor at all levels are shown in Tables 3 and 4.

From Table 4. it is observed that two sets of parameter combinations satisfy the optimization design requirements. The best combination for minimizing the detent force is L_{pm_1}(1), w_{pm_k}(1), dy(2), w_{fx}/(2), and h_{fz}(2), On the other hand, for maximizing the thrust force, the optimal
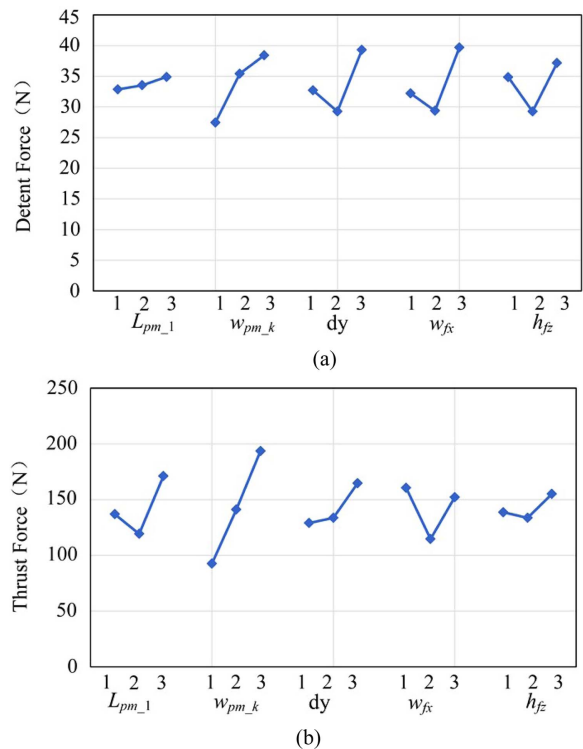

Fig. 8. (Color online) Output performance effect by different parameters. (a) Detent force effect by different parameters, (b) Thrust force effect by different parameters.

Table 5. Proportion effect on each parameter.

Parameters	F_d/N		F_t/N	
	S_q.	ratio, %	S_q.	ratio, %
L_{pm_1}/mm	0.71	1.02	464.17	16.02
w_{pm_k}/mm	21.41	30.81	1701.91	58.72
dy/mm	17.35	24.97	251.59	8.68
w_{fx}/mm	19.01	27.37	396.67	13.69
h_{fz}/mm	10.99	15.82	83.79	2.89

combination is $L_{pm\_1}(3)$, $w_{pm\_k}(3)$, dy(3), $w_{fx}/(1)$, and $h_{fz}(3)$. To evaluated the effect of parameters on the motor performances, variance is employed and can be calculated using the following equation:

$$S_q = \frac{1}{Q}\sum_{k=1}^{Q}(M_{p(k)} - M)^2 \qquad (14)$$

where, Q is the number of levels, P represents the different factors, $M_{p(k)}$ is the mean value of performance under the level kth, M is shown in Table 4.

According to the mean and variance values, the main factors affecting the performance of T-LPMM are depicted in Fig. 8, and their corresponding proportions are provided in Table 5.

Table 5 reveals that L_{pm_1} exhibit sensitivity to the thrust force (F_t), while w_{pm_k} significantly influences both F_t and the detent force (F_d). Additionally, dy, w_{fx} and h_{fz} have a notable impact on F_d. Based on the analysis, the final optimized parameters for T-LPMM are determined and shown in Table 6.

5. Validation

To verify the analytical method proposed in this paper, the FEA method and test are carried out on T-LPMM.

The flux lines distribution at the typical positions are illustrated in Fig. 9. According to the principle of minimum reluctance, the flux line starts from the N pole of PM,
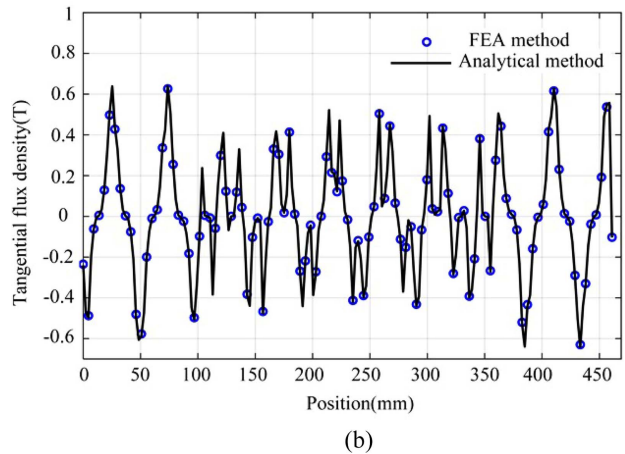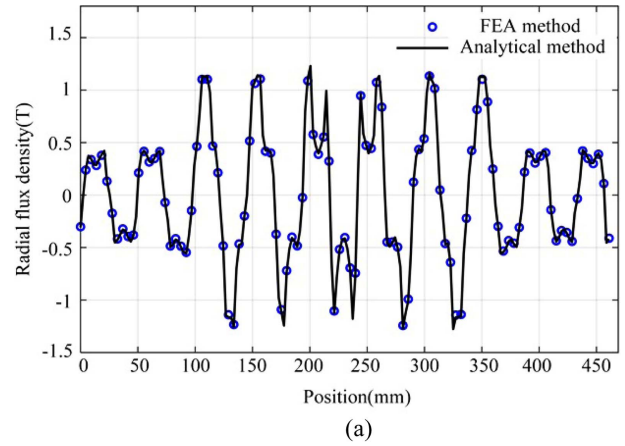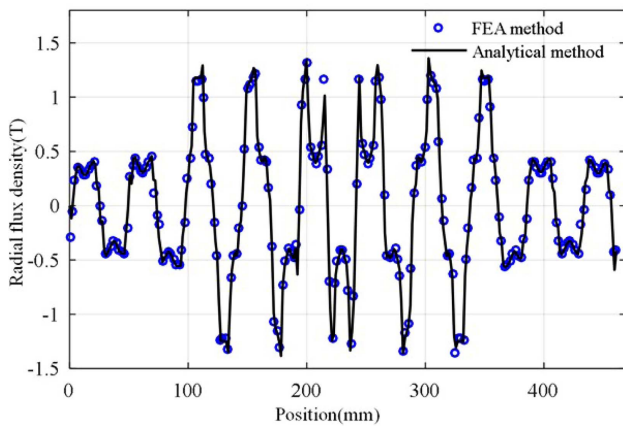

(a)

(b)

Fig. 10. (Color online) Air-gap magnetic field distribution with slot effect under no-load condition. (a) Radial flux density distribution of T-LPMM, (b) Tangential flux density distribution of T-LPMM.
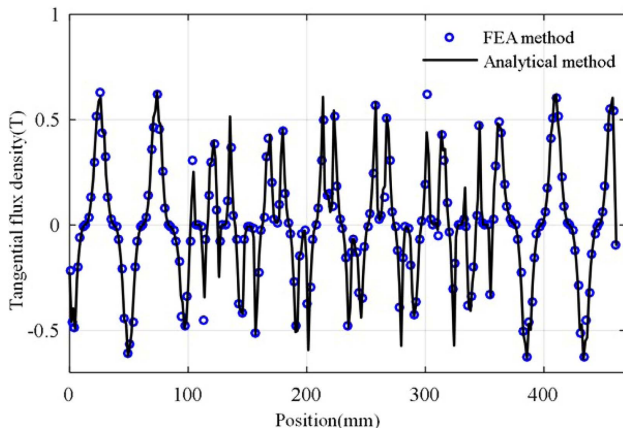
Table 6. Optimal combination parameters of T-LPMM.

Level combination	L_{pm_1} (3) w_{pm_k}(3) dy (2) w_{fx}(2) h_{fz}(2)				
Parameters	L_{pm_1}/mm	w_{pm_k}/mm	dy /mm	w_{fx} /mm	h_{fz}
	17	3	1	29	10

Fig. 9. (Color online) Flux line distribution of T-LPMM at a typical position.

passes through the stator teeth and yoke, then returns to the S pole.

5.1. FEA Validation

Fig. 10 shows the results of the comparison between the analytical and FEA method for the slotless air-gap magnetic flux density distribution when the mover is positioned at a specific location. The end effect, auxiliary teeth effect and slot effect are all considered. From Fig. 10, it can be observed that, the analytical solutions closely align with the FEM results, demonstrating good accuracy. The maximum radial flux density in the auxiliary teeth region slightly exceeds that in the end region, measuring approximately 0.52 T. The tangential flux density ranges from 0.02 to 0.48 T. In the slot region, the radial flux density ranges from -1.24 to 1.24 T, while the maximum tangential flux density reaches around 0.58 T. The small discrepancies may be attributed to the crowding effect of SC mapping in the analytical model.

Fig. 11 compares the analytical and FEM results of the armature reaction field in the air-gap region for a specific position. Excellent agreement between the two methods is achieved. The radial magnetic flux density value in the end region is noticeably smaller than that in the iron area, varying from -0.46 to 0.46 T. Conversely, the tangential magnetic density distribution is opposite, with the end region having higher values of approximately 0.62 T compared to the iron area. In the slot region, the radial magnetic flux density value can reach up to 1.4 T.

6. Comparison

To further verify the electromagnetic performance of the proposed T-LPMM, a comparison is made with SM-LPMM at the same volume, external radius and running speed. The main parameters were given in Table 6, and the test platform is shown in Fig. 12.
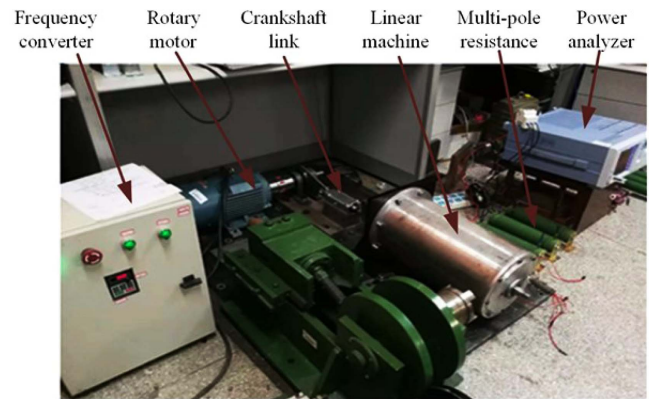
Fig. 13 illustrates the comparative distribution of EMF

(a)

(b)

Fig. 11. (Color online) Air-gap magnetic field distribution with slot effect under load condition. (a) Radial flux density distribution of T-LPMM, (b) Tangential flux density distribution of T-LPMM.

Fig. 12. (Color online) Comparison test platform between T-LPMM and SM-LPMM.
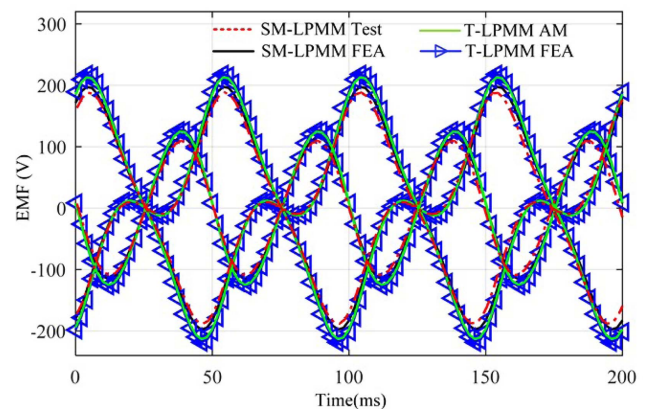

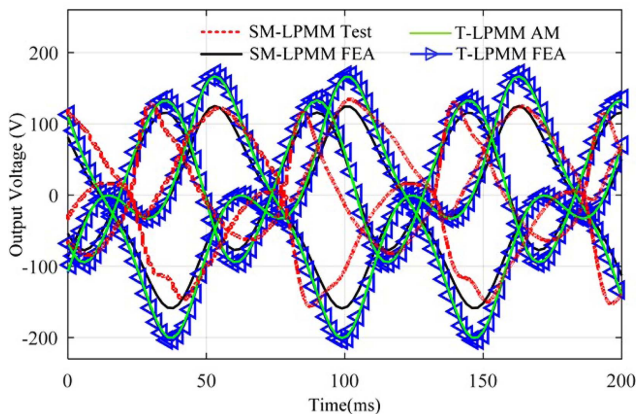**Fig. 13.** (Color online) Comparison of voltage under open condition.

Fig. 14. (Color online) Comparison of voltage under load condition.
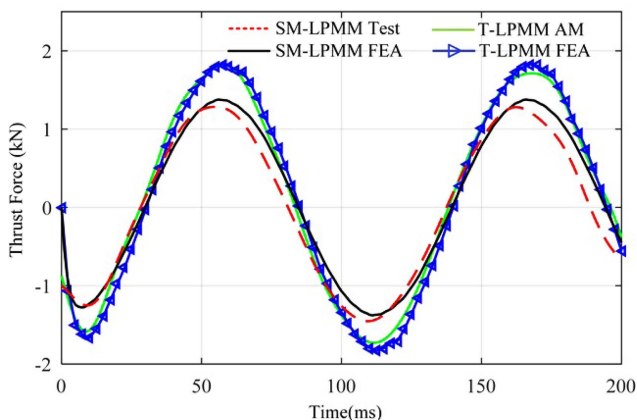

Fig. 15. (Color online) Comparison of thrust force between T-LPMM and SM-LPMM.

under open-circuit conditions when two linear machines operate at the same speed. From Fig. 13, it can be observed that the maximum voltage of SM-LPMM is 316.54 V, while the proposed T-LPMM achieves a significantly improved value of 415.65 V. The non-sinusoidal nature of EMF is attributed to the reciprocating motion of the mover at a sinusoidal speed within a polar pitch.

Figs. 14 and 15 compare the output voltage and thrust force distributions of the two linear machines at a resistance of R=50 Ω. T-LPMM exhibits an output voltage of 357.8 V, while SM-LPMM yields 267.4 V. Simultaneously, the thrust force of T-LPMM measures 500 N, which is twice that of the traditional linear machine.

7. Conclusion

The study highlights the development of an improved T-LPMM, with various advantages such as high thrust force, low magnetic flux leakage, and enhanced protection for PM in special application environments. The research employed a combination of FEM and MATLAB to predict the slotless magnetic field, taking into account the end effect. Additionally, SC mapping was conducted to calculate the slot effect, considering auxiliary teeth. The armature reaction was analyzed using an established SD model. To optimize the parameters of T-LPMM, Taguchi method was utilized. The analytical results were verified through FEM and experimental tests, demonstrating good agreement between the predicted and actual magnetic flux densities, as well as the electromagnetic performance of the machine. However, during testing, a phase deviation was observed, which was attributed primarily to vibrations in the iron block connecting T-LPMM to the crankshaft connecting rod device.

References

[1] J. Prudell, M. Stoddard, E. Amon, T. K. A. Brekken, and A. von Jouanne, IEEE Trans. Ind. Appl. **46**, 2392 (2010).
[2] Z. Zhang, B. Wu, Q. Lu, and W. Xu, in 2021 13th International Symposium on Linear Drives for Industry Applications (LDIA), Wuhan, China, Jul. 2021, pp. 1-6.
[3] L. Yan, Z. Dong, and S. Zhang, IEEE Trans. Energy Convers. **37**, 1042 (2022).
[4] L. Zhang et al., IEEE Trans. Energy Convers. **36**, 3522 (2021).
[5] Y. Amara, G. Barakat, and P. Reghem, IEEE Trans. Magn. **47**, 805 (2011).
[6] S. Qiu, W. Zhao, C. Zhang, J. K. H. Shek, and H. Wang, IEEE Trans. Energy Convers. **37**, 24 (2022).
[7] N. Hodgins, O. Keysan, A. S. McDonald, and M. A. Mueller, IEEE Trans. Ind. Electron. **59**, 2094 (2012).
[8] T. Xia, H. Yu, R. Guo, and X. Liu, IEEE Trans. Appl. Supercond. **28**, 1 (2018).
[9] Z. Liao, J. Yue, and G. Lin, IEEE Trans. IEEE Trans. Appl. Supercond. **31**, 1 (2021).
[10] K.-H. Shin, H.-I. Park, J.-M. Kim, H.-W. Cho, and J.-Y. Choi, IEEE Trans. Magn. **52**, 1 (2016).
[11] K.-H. Shin, K.-H. Jung, H.-W. Cho, and J.-Y. Choi, IEEE Trans. Magn. **54**, 1 (2018).
[12] M.-G. Park, J.-Y. Choi, H.-J. Shin, K. Lee, and K. Hong, IEEE Trans. Magn. **50**, 1 (2014).

[13] M. M. Ali, W. Xu, A. Junejo, M. Elmorshedy, and Y. Tang, IEEE Trans. Energy Convers. **37**, 795 (2022).

[14] M. Ghods, J. Faiz, M. A. Bazrafshan, and M. H. Arianborna, IEEE Trans. Energy Conversion **37**, 1087 (2022).

[15] R. Guo, H. Yu, and B. Guo, IEEE Transactions on Transportation Electrification **6**, 602 (2020).

[16] M. Ma, Z. Xu, Z. Xu, Y. Zhang, and Z. Wang, IEEE Trans. Energy Convers. 11, (2022).

[17] L. J. Wu, Z. Q. Zhu, D. A. Staton, M. Popescu, and D. Hawkins, IEEE Trans. Ind. Electron. **59**, 2414 (2012).

[18] K. Ramakrishnan, M. Curti, D. Zarko, G. Mastinu, J. J. H. Paulides, and E. A. Lomonova, IET Electric. Power Appl. **11**, 540 (2017).

[19] S. Xu, X. Liu, and Y. Le, IEEE Trans. Magn. **53**, 1 (2017).